Spin polarization and exchange coupling of Cu and Mn atoms in paramagnetic CuMn diluted alloys induced by a Co layer

M. Abes,[*] D. Atkinson, and B. K. Tanner
Department of Physics, University of Durham, South Road, Durham DH1 3LE, United Kingdom

T. R. Charlton and Sean Langridge[†]
ISIS, Rutherford Appleton Laboratory, Harwell Science and Innovation Campus, Oxon OX11 0QX, United Kingdom

T. P. A. Hase
Department of Physics, University of Warwick, Coventry CV4 7AL, United Kingdom

M. Ali, C. H. Marrows, and B. J. Hickey
School of Physics and Astronomy, University of Leeds, Leeds LS2 9JT, United Kingdom

A. Neudert[‡] and R. J. Hicken
School of Physics, University of Exeter, Exeter EX4 4QL, United Kingdom

D. Arena
National Synchrotron Light Source, Brookhaven National Laboratory, Upton, New York 11973-5000, USA

S. B. Wilkins
Condensed Matter Physics and Materials Science Department, Brookhaven National Laboratory, Upton, New York 11973-5000, USA

A. Mirone
European Synchrotron Radiation Facility, BP 220, F-38043 Grenoble Cedex, France

S. Lebègue
Laboratoire de Cristallographie, Résonance Magnétique, et Modélisations, CRM2, UMR CNRS 7036, Institut Jean Barriol, Nancy Université, BP 239, Boulevard des Aiguillettes, 54506 Vandoeuvre-lès-Nancy, France

Using the surface, interface, and element specificity of x-ray resonant magnetic scattering in combination with x-ray magnetic circular dichroism, we have spatially resolved the magnetic spin polarization, and the associated interface proximity effect, in a Mn-based high-susceptibility material close to a ferromagnetic Co layer. We have measured the magnetic polarization of Mn and Cu $3d$ electrons in paramagnetic CuMn alloy layers in $[Co/Cu(x)/CuMn/Cu(x)]_{20}$ multilayer samples with varying copper layer thicknesses from $x=0$ to 25 Å. The size of the Mn and Cu $L_{2,3}$ edge dichroism shows a decrease in the Mn-induced polarization for increasing copper thickness indicating the dominant interfacial nature of the Cu and Mn spin polarization. The Mn polarization is much higher than that of Cu. Evidently, the Mn moment is a useful probe of the local spin density. Mn atoms appear to be coupled antiferromagnetically with the Co layer below $x=10$ Å and ferromagnetically coupled above. In contrast, the interfacial Cu atoms remain ferromagnetically aligned to the Co layer for all thicknesses studied.

PACS number(s): 72.25.Mk, 75.25.−j, 85.75.−d

I. INTRODUCTION

Spin-dependent electron-transport phenomena such as giant magnetoresistance, domain-wall magnetoresistance, and magnetization-reversal processes induced by transverse spin injection,[1,2] in ferromagnetic/nonmagnetic structures, show intriguing characteristics associated with interfacial phenomena. Devices based on spin transport effects have great advantages over conventional electronic devices because of the additional spin functionality.[3] This functionality is often interface dominated. Of utmost relevance for spin transport is the length scale over which the electron spin retains its initial polarization direction. This is known as the spin diffusion length (λ_{sf}) and its magnitude has been the subject of some debate.[4,5] Clearly to understand such systems requires a detailed quantitative knowledge of the spatial distribution of the magnetization. This is experimentally challenging given that the polarization may be small, located at a buried interface and in proximity to material with a much larger magnetization. Nonetheless, experimentally determining the spatial polarization has widespread significance in areas such as Ruderman-Kittel-Kasuya-Yoshida (RKKY) interlayer coupling,[6–8] induced proximity magnetism[9] and in the case of spin injection, the driven accumulation[10,11] of spin at an interface. Understanding the mechanisms behind the equilibrium and out-of-equilibrium magnetization becomes important to the future realization and technological exploitation of

spin-electronic devices, in particular, the lengthscale over which the spin functionality can be transported.

In several cases (RKKY, proximity magnetization, and spin accumulation) the magnitude of the induced magnetization is small, typically of order 0.01 μ_B per atom with a spatial extent localized close to the interfacial region. By establishing a methodology to observe these small polarizations in an equilibrium (proximity) system we expect that such ideas can be extended to the, out-of-equilibrium, driven case of spin accumulation.

We have undertaken x-ray resonant magnetic scattering (XRMS) measurements combined with x-ray magnetic circular dichroism (XMCD) to study the proximity effect by determining the moment of delta-doped[12] high-susceptibility impurities in close proximity to a ferromagnetic layer. The interface sensitivity of the XRMS technique is ideal for characterizing the spatial extent of the spin polarization.[13–17] As part of this work we have used hard x-ray reflectivity to provide a structural characterization of the sample.

To enhance the interfacial sensitivity we chose to study the polarization of Mn atoms in a paramagnetic CuMn alloy with a 50% Mn concentration. Mn is an ideal choice as electronic band-structure calculations have shown that the Mn atoms possess almost a 100% spin polarization at the Fermi level.[18,19]

In this paper, we focus on the interface effect which, through the contact between Co, Cu, and Mn atoms, favors a direct hybridization and therefore induces ferromagnetism in Mn and Cu. We investigate the Cu and Mn 3d magnetic profiles in a $[Co/CuMn(20\ \text{Å})]_{20}$ multilayer (ML) where there is direct contact between the ferromagnet and the paramagnetic layers.[19] To spatially resolve the magnetic profile we have also studied the Cu and Mn magnetic profiles in $[Co/Cu(x)/CuMn/Cu(x)]$ MLs. Here a delta layer of Cu (x Å thick) has been inserted at the interfaces to separate the Mn and Co atoms. The magnetic profile is then modeled by fitting the x-ray data using a calculation based on the Fresnel formalism.[20]

This study is organized as follows: the outline theory of XRMS is presented in Sec. II. The experimental details and growth of the multilayers are summarized in Sec. III. The experimental and theoretical results are compared with the calculated reflectivity spectra and presented in Sec. IV and discussed in Sec. V.

II. X-RAY RESONANT MAGNETIC REFLECTIVITY

During the last three decades, magnetic soft x-ray spectroscopy techniques have become an increasingly valuable tool in the characterization of the magnetic properties in materials. These activities were stimulated by the observation of strong dichroic effects in absorption, transmission, or scattering experiments in the vicinity of the 2p edges of the 3d transition metals.[21,22] Among these techniques, x-ray resonant magnetic scattering has received considerable attention and offers several specific advantages compared to absorption or transmission measurements. It combines the benefits of magnetic dichroism with a scattering technique and enables the determination of the spatial profile of the magneti-

zation through the layers. The dichroic effects can exceed the magnitude of corresponding effects in photoabsorption and benefit from a much larger probe depth.[21] However, since the reflectivity depends on the experimental geometry and the morphology of the sample (e.g., layer thicknesses and roughnesses), a detailed analysis of spectroscopic reflectivity data requires a more sophisticated numerical treatment than that associated with the analysis of photoabsorption data. Nevertheless, experiment and simulation demonstrate the promising potential of reflectivity analysis.[23,24]

At the Cu and Mn $L_{2,3}$ edges, the dichroic signal results from electric dipole transitions from the 2p atomic core level to the unoccupied 3d states which support the magnetic moment. As with XMCD, the magnetic sensitivity arises from the exchange splitting of the unoccupied 3d states induced by their magnetic polarization and from the spin polarization of the photoelectron which is related to the spin-orbit coupling in the 2p core level. Here we only cite the pertinent expressions relevant to the interpretation of our experimental results.

The resonant x-ray atomic scattering factor of a magnetic atom can be written in the dipole approximation as[25]

$$f(E) = (\hat{\varepsilon}_f^* \cdot \hat{\varepsilon}_i)F^0(E) - i(\hat{\varepsilon}_f^* \times \hat{\varepsilon}_i) \cdot \hat{y}F^1(E) \qquad (1)$$

with the charge- and magnetization-dependent scattering amplitudes

$$F^0(E) = f_0 + f'(E) + if''(E), \qquad (2)$$

$$F^1(E) = m'(E) + im''(E), \qquad (3)$$

respectively. Here E is the energy of the incident x rays, $\hat{\varepsilon}_i$ and $\hat{\varepsilon}_f$ are the unit polarization vectors of the incident and scattered x rays, respectively, and $\hat{y}$ is the magnetization unit vector. f_0 is the tabulated atomic scattering factor[26] and $f'(E)$ and $f''(E)$ are the real and imaginary parts of the complex resonant anomalous scattering factor, respectively. In Eq. (3), $m'(E)$ and $m''(E)$ are the real and imaginary parts of the resonant magnetic scattering factor. Beyond the region for total external reflection we can define complex charge $F(\vec{q},E)$ and magnetic structure $\hat{M}(\vec{q},E)$ factors[23]

$$F(\vec{q},E) = \sum_j F^0(E)e^{i\vec{q}\cdot\vec{r}_j}, \qquad (4)$$

$$\hat{M}(\vec{q},E) = \sum_j \hat{y}_j F^1(E)e^{i\vec{q}\cdot\vec{r}_j}. \qquad (5)$$

In order to determine the profile of the magnetization of a layer, particularly one whose polarization is strongly thickness dependent, the number of atomic planes, their interplanar distances, and concentrations are obtained directly from the analysis of conventional, nonresonant hard x-ray diffraction, and reflectivity data. Once the chemical/electronic structure has been determined to sufficient precision, it is possible to fit the element-specific XRMS in order to extract the magnetic profile of the Mn and Cu layers. The intensities observed in elastic scattering are then related to the square of the total structure factor to yield cross terms that represent the resonant magnetic-charge interference scattering. This
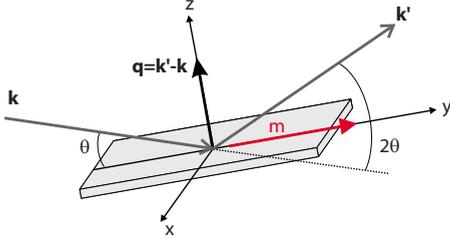
FIG. 1. (Color online) Schematic of the longitudinal geometry used in the XRMS measurements. $\vec{k}$ and $\vec{k}'$ are the wave vectors of the incoming and outgoing circularly polarized x rays, respectively. $\vec{m}$ is the magnetization of the sample. The applied field $\vec{H}$ is parallel to the y axis.

magnetic cross term can be accessed by taking the difference of the observed intensity, $(I^{\pm})$, by either changing the helicity of the incident circularly polarized photons or reversing the magnetization within the sample

$$I^+ - I^- = -2(\hat{k} + \hat{k}' \cos 2\theta)(F'\hat{M}' + F''\hat{M}''), \qquad (6)$$

where F and $\hat{M}$ are written as sums of the real and imaginary parts

$$F(\vec{q},E) = F' + iF'', \qquad (7)$$

$$\hat{M}(\vec{q},E) = \hat{M}' + i\hat{M}'', \qquad (8)$$

where F', F'', $\hat{M}'$, and $\hat{M}''$ are real quantities for centrosymmetric structures. In our measurements the magnetic field was applied parallel and antiparallel to the direction defined by the sample plane and the scattering plane as shown in Fig. 1. In Fig. 1, the y-z plane is parallel to the plane of x-ray scattering, defined by the incident and scattered wave vectors $\vec{k}$ and $\vec{k}'$, and the $+z$ axis is parallel to the outward normal of the multilayer surface. In specular reflection, $\vec{k}$ and $\vec{k}'$ make angles $-\theta$ and θ to the $+y$ axis, respectively, which is along $\vec{k}+\vec{k}'$.

The scattered intensity was modeled by adapting Parratt's recursion formula[27] for nonmagnetic specular reflectivity from a multilayer. The refractive index for layer j is $n_j^{\pm} = 1 - \delta_j^{\pm} + i\beta_j^{\pm}$ for each of the applied magnetic field directions $(\pm)$. The refractive indices are related to f and m for the forward scattering by

$$\delta^{\pm} = \left(\frac{2\pi n_0 r_e}{k^2}\right)[f_0 + f'(E) \mp m'(E)\cos\theta], \qquad (9)$$

$$\beta^{\pm} = \left(\frac{2\pi n_0 r_e}{k^2}\right)[f''(E) \mp m''(E)\cos\theta], \qquad (10)$$

where n_0 is the number of atoms per unit volume and r_e is the electron classical radius. In practice it is often convenient to decompose the measured quantities into the magnetic and nonmagnetic contributions

$$\delta^{\pm} = \delta_0 \mp \Delta\delta, \qquad (11)$$

$$\beta^{\pm} = \beta_0 \mp \Delta\beta. \qquad (12)$$

The absorptive charge and magnetic components, β_0 and $\Delta\beta$, are then proportional to the measured linear absorption coefficient $\mu^{\pm}(E)$ through the optical theorem.

III. EXPERIMENTAL DETAILS

Polycrystalline samples were prepared at the University of Leeds, by dc magnetron sputtering operating at a base pressure of 5×10^{-8} Torr at room temperature. In order to enhance the (111) texturing the multilayers were grown on Ta buffer layers deposited onto silicon substrates and were sputtered at growth rates of 2.3 Å/s, 4.2 Å/s, and 3.9 Å/s for Co, $Cu_{50}Mn_{50}$, and Cu, respectively, in an argon atmosphere of 2.5 mTorr. The samples were protected from oxidation by a 15 Å Al capping layer.

Six samples were grown in the same vacuum cycle with nominal structures,

$$Si(100)/Ta(200 \text{ Å})/[Co(40 \text{ Å})/Cu(x)/Cu_{50}Mn_{50}(20 \text{ Å})/Cu(x)]_{20}/Al(15 \text{ Å})$$

with $x=0$, 5, 10, 15, 20, and 25 Å. We shall refer to these samples as Co/Cu(x)/CuMn. All samples had an in-plane easy magnetization axis. The Co layers saturate below 400 Oe with a remanent in-plane magnetization at nearly 100% of the saturation magnetization.

XRMS and XMCD experiments were performed on a two-circle diffractometer with a vertical scattering geometry in a high vacuum chamber on station 5U1 at the Daresbury SRS. Energies in the range of 200–1400 eV with a resolution of ≈ 150 meV and flux of typically 10^{10} photons/sec/100mA were available. A magnetic field was applied in the scattering plane along the sample surface. This corresponds to the ge-

ometry employed in the longitudinal magneto-optical Kerr effect. The maximum field of ± 500 Oe was large enough to fully saturate the Co layer in all samples. By tuning the photon energy to the absorption edge of interest, a scan of the reflected intensity is performed as a function of scattering vector. For each scattering vector an asymmetry ratio can be defined $R=(I^+ - I^-)/(I^+ + I^-)$. A measurement of the energy-dependent asymmetry ratio at a fixed scattering vector $\vec{q}$ is sufficient to separate the structural and magnetic contributions to the scattered intensity. For the measurements of the absorptive parts (XMCD), the photon incident angle was set at 70°.

The analysis of the multilayer magnetization profile is performed within the pythonic program for multilayers (PPM) software.[28] In order to determine the structure of the samples, hard x-ray reflectometry measurements were recorded on X22B at the National Synchrotron Light Source, Brookhaven National Laboratory at an energy of 8.9 keV. Specular scans (q_z scan) provide information on the near-surface electron density and total interface width. They do not distinguish between compositional grading and true roughness as there is no component of scattering vector in the surface.

Transverse diffuse scans (q_x scan at fixed q_z) allow the total interface width (σ_{rms}), determined from the specular scans to be subdivided into topological roughness and compositional grading components.[29] The transverse diffuse scan is sensitive to the in-plane structure of the interfaces and by simulating the diffuse data, the in-plane correlation length, ξ, and the fractal parameter h can be determined. The h parameter can take values between 0 and 1 and is related to the fractal dimension of the surface and describes the jaggedness of the interface. Off-specular (longitudinal diffuse) scans were performed in which the scattering geometry is the same as that of the specular scan but with a small offset ($-0.1°$) in the sample angle. These longitudinal scans in reciprocal space, which probe the diffuse scatter close to the specular ridge, are necessary in order for the true specular scatter to be obtained by subtraction of the diffuse scatter from the measured specular scatter. They also permit us to determine the degree of conformal roughness, Kiessig fringes, and Bragg peaks in the diffuse scatter arising only from the presence of roughness that replicates through the multilayer structure.

IV. RESULTS

A. Hard x-ray reflectometry

A series of grazing incidence true specular scans for the MLs are shown in Fig. 2(a). The Bragg peaks due to the periodicity of the MLs are clearly visible in the specular reflectivity spectra at ≈ 0.1 Å^{-1}, which agree with the nominal sample periodicity. In addition to the Bragg peaks the presence of well-defined finite-thickness oscillations (Kiessig fringes) clearly indicates a well-ordered layered structure. The off-specular Bragg peaks remain (not shown), indicating that the out-of-plane correlation is retained within the multilayer. The specular scatter of the multilayers was modeled using the Bede REFS-MERCURY software which uses a genetic algorithm to refine a model structure to the experimental data by an iterative cominimization process.[29,30] Values of thickness and interface width were first found using this code for the specular data and these parameters then used to fit the diffuse scatter manually [Fig. 2(b)]. Best fits to the experimental data are included in the figures. In all cases we were able to obtain good fits between the simulated and experimental data, the results for the MLs being shown in Table I. Transverse diffuse data taken at the second Bragg peak for all samples [as in example Fig. 2(b) on the Co/CuMn multilayers] and the associated simulations show that there is no or very small detectable interdiffusion contribu-
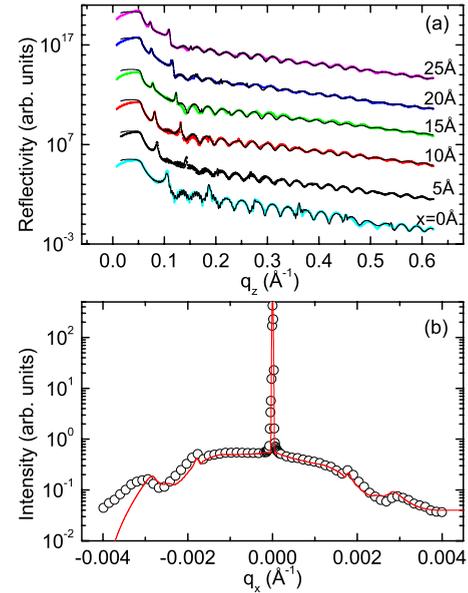
FIG. 2. (Color online) (a) Specular reflectivities of the Co/Cu(x)/CuMn multilayers. The data sets are offset on the ordinate axis for display purposes. (b) Representative transverse scan of the Co/CuMn ($x=0$) sample measured on the second Bragg peak. The solid line (best fit) is calculated using $h=1/2$, $\sigma=5.5$ Å, and $\xi=140$ Å. The experimental data are shown as symbols and the calculated reflectivity is represented by the solid lines. The measurements are realized with hard x rays ($E=8.9$ keV).

tion to the interface width between the CuMn/Co, Co/CuMn, Cu/Co, and Co/Cu layers in any of the samples and all of the effective roughness corresponds to rms topological roughness. The in-plane correlation length of the roughness morphology was determined to be in the region of a few hundred Angstroms and the fractal parameter is ≈ 0.5. The rms topological roughness values are approximately 5 Å for all CuMn/Co, Co/CuMn, Cu/Co, Co/Cu, CuMn/Cu, and Cu/CuMn interfaces. The amplitude of the in-plane correlation length and the topological roughness are in agreement with previous observations in Co/Cu multilayers grown by magnetron sputtering[31,32] while the jaggedness of the interfaces shows no significant difference.

B. Soft x-ray reflectometry

The incident-photon-flux normalized transmission x-ray absorption spectroscopy (XAS) spectra of cobalt, manganese, and copper are taken from a Co(50 Å)/Cu(5 Å)/CuMn(20 Å) sample. The applied magnetic field direction was along the intersection of the incidence plane and the sample surface plane. The relative absorption cross sections from the transmission spectra have been deduced using the method of Chen *et al.*[33] After taking into account the incident photon angle of 70° and the degree of circular polarization of 100% (i.e., multiplying $\mu^+ - \mu^-$ by $\frac{1}{\cos(70)}$ while keeping $\mu^+ + \mu^-$ the same), the resulting $\mu^\pm(E)$, $\mu^+(E) - \mu^-(E)$ (the XMCD difference spectra), and $\mu^+(E) + \mu^-(E)$ (the XAS sum spectra) are deduced. The resulting (electronic) β_0 and $\Delta\beta$ (magnetic) contributions to the imagi-

TABLE I. Best-fit parameters for the specular reflectivity of the $Co/Cu1(x)/CuMn/Cu2(x)$ multilayers.

	Thickness				Interface morphology			
x	**Co,** ± 1 Å	**Cu1,** ± 0.5 Å	**CuMn,** ± 0.5 Å	**Cu2,** ± 0.5 Å	$\sigma_{topological}$, ± 0.5 Å	$\sigma_{grading}$, ± 0.5 Å	ξ, ± 20 Å	h, ± 0.1
0	42		23.5		5.5	1.0	140	0.5
5	41	6.5	22.5	5.5	4.0	0.5	170	0.5
10	41	12.0	19.5	11.5	5.0	1.0	220	0.5
15	43	16.5	23.0	17.5	5.5	0.5	180	0.5
20	39	22.5	20	21.0	5.5	0.5	180	0.5
25	43	27.0	22.5	28.5	6.0	1.0	250	0.5

nary part of the refractive index are shown as solid lines in Fig. 3 for Mn and Co. The real parts δ_0 and $\Delta\delta$ (shown as dashed lines in Fig. 3) have been obtained using the Kramers-Kronig transformation (KKT). Note that the $\Delta\beta$ contribution of the Mn has been smoothed since the experimental data was noisy. According to the sum rules, the orbital and spin magnetic moments can be determined from the XAS and XMCD spectra. The experimental values deduced from the sum rules are 1.50 ± 0.10 μ_B and 0.21 ± 0.04 μ_B corresponding to the Co spin and orbital moments, respectively. A small dichroism signal is detected at the $L_{2,3}$ edges of the manganese while no dichroism is observed at the $L_{2,3}$ edges of the copper. In order to simulate our data from the XRMS, the dichroic signals at the Cu $L_{2,3}$ edges are taken from $Co/Cu(10$ Å$)$ multilayers.[34] From the XMCD and XAS spectra the value of the spin magnetic moment can, in principle, be obtained via the sum rules. The Cu moment is extracted from the data following Samant *et al.*[34] This results in a derived Cu moment of 0.10 ± 0.02 μ_B. However, the sum-rule analysis becomes problematic for Mn because the

$2p$-$3d$ electrostatic interactions are relatively large compared to the $2p$ spin-orbit interaction. This causes the manifolds of the $2p_{3/2}$ and $2p_{1/2}$ levels to overlap strongly and, consequently, there is a substantial amount of mixing between these two j levels. The correction factor needed to extract a meaningful magnetic moment from the sum rules is $\chi = 1.5$.[35,36] From the correction of these sum rules, the Mn moment extracted is 0.05 ± 0.01 μ_B. The dichroic signal is generally rather weak and noisy resulting in a rather large ambiguity on the final Mn moment. We can compare our sum-rules analysis with the XMCD amplitudes available in the literature. The amplitude of the L_3 XMCD signal amplitude in our case represents 0.03% of the absorption signal. In the case of fcc Mn/Co(001) system, a 36% amplitude of the XMCD signal was assigned to 4.5 μ_B, (or 8% XMCD/μ_B).[37] For the bcc Mn/Fe(001) systems, the following percentages of XMCD/μ_B have been reported: 8%,[38] 9.2%,[39] and 7.4%.[40] Assuming that an average value of $8 \pm 1\%$ L_3 XMCD signal corresponds to 1 μ_B, we obtain from our spectra a magnetic moment for the Mn atoms of (0.04 ± 0.02) μ_B. This value is in agreement with our more rigorous sum-rules analysis and given the uncertainties in applying this analysis to Mn it provides confidence for the extracted value for Mn in a wide range of environments.

Figure 4 displays the specular x-ray resonant reflectivity
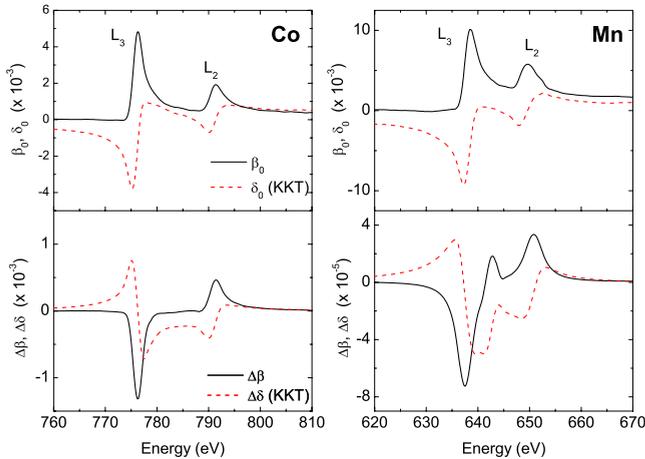
FIG. 3. (Color online) Optical constants of the Co and Mn layers in the vicinity of the $2p$ edges determined by means of XAS and XMCD (black solid lines) and subsequent KKT (dashed lines) as described in the text. The top left panel shows the Co nonmagnetic (purely electronic) imaginary, β_0 and real part δ_0 of the index of refraction. The magnetic imaginary $\Delta\beta$ and real contribution $\Delta\delta$ are shown in the lower left panel. The right panel presents the equivalent data for Mn.
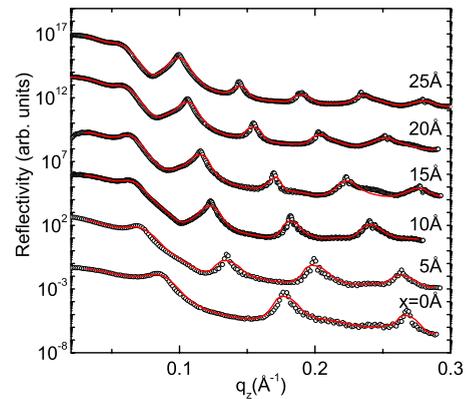
FIG. 4. (Color online) Reflectivity of the $Co/Cu(x)/CuMn$ multilayers measured with circularly polarized soft x rays ($E = 780$ eV) as a function of copper thickness (see legend). The experimental data are shown as the open black circles and the calculated reflectivity is represented by the solid line.
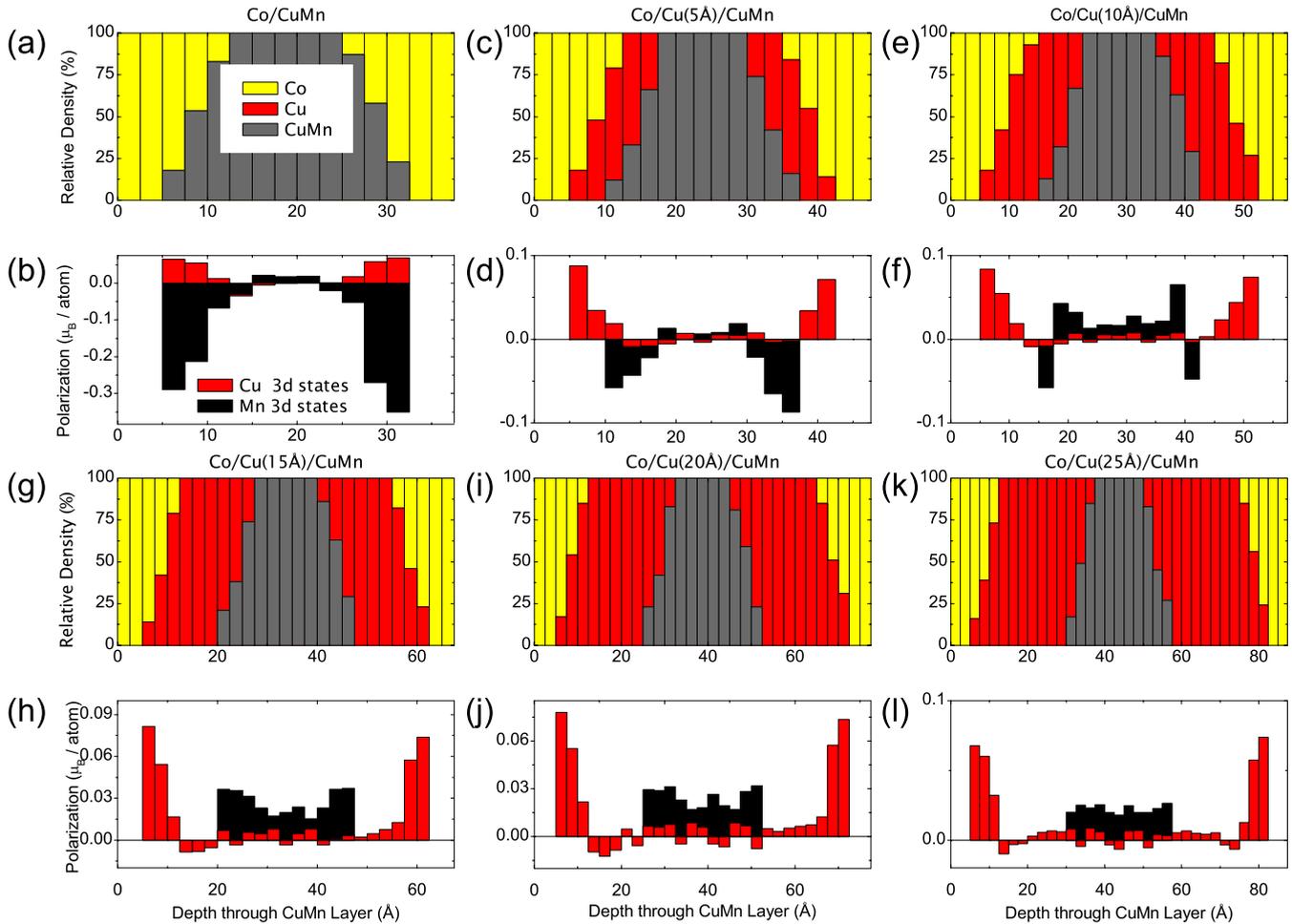
FIG. 5. (Color online) Profiles of the relative Co, Cu, and CuMn densities as a function of CuMn layer depth are shown in panels (a), (c), (e), (g), (i), and (k). The errors in the relative density are estimated as ± 0.1. Panels (b), (d), (f), (h), (j), and (l) present the profiles of the Cu and Mn polarizations, given in units of μ_B/Cu and μ_B/Mn.

measurements for Co/Cu(x)/CuMn/Cu(x) multilayers sitting just above the Co L_3 edge ($E = 780$ eV) where the magnetic contribution of the absorptive part is maximum. The solid lines passing through the reflectivity data are the best fit and although the fit of the individual curves is not perfect, the intensity changes from Bragg peak to Bragg peak have been satisfactorily reproduced. In contrast to the fitting strategy for the hard x-ray data where the layers were considered as individual fitting elements, in these simulations, we have divided the layer into slices along the out-of-plane z direction approximately one atomic plane in thickness (≈ 2.5 Å). The interfacial structures were then modeled by varying the relative densities of Co, Cu, and CuMn densities through the sample. Note that for the specular reflectivity, we cannot distinguish between a topologically rough and a compositionally graded interface. The relative densities of the Co, Cu, and CuMn within the bilayer or trilayer are shown in panels (a), (c), (e), (g), (i), and (k) of Fig. 5 for multilayers with a Cu spacer thickness of $x = 0$ Å, 5 Å, 10 Å, 15 Å, 20 Å, and 25 Å, respectively. The density profiles show extended regions on either side of the central CuMn layer, which consist of a mixture of Co and CuMn atoms at $x = 0$ Å and Cu and Co atoms at $x > 0$. Error bars in these figures are esti-

mated at 0.1 along the ordinate axis. These alloy-type regions account for the effects of interfacial roughness and interdiffusion that can alter the profile of the magnetization.

We collected energy-dependent XRMS data at the Cu and Mn $L_{2,3}$ edges from Co/Cu(x)/CuMn multilayers for a fixed scattering vector. The energy dependence of the asymmetry ratios recorded at the Cu and Mn $L_{2,3}$ edges are shown in Figs. 6 and 7, respectively, for all samples, at a fixed scattering vector corresponding to a position of a maximum in the asymmetry ratio at a fixed energy. The asymmetry ratios at the Cu and Mn $L_{2,3}$ edges exhibit a dichroism effect, unambiguously demonstrating a magnetic polarization of the Cu and Mn 3d electrons. The dichroism effect is observed for all samples but weakens with increasing Cu thickness. We note that no dichroism is observed at the Cu and Mn $L_{2,3}$ edges for a pure CuMn ($x = \infty$) sample as shown in Figs. 6 and 7 indicating that the magnetic polarization observed at the Cu and Mn $L_{2,3}$ edges for Co/Cu(x)/CuMn/Cu(x) multilayers samples are induced by the Co layer. The effective field from the Co induces a small Mn ferromagnetic component through a partial alignment of the Mn paramagnetic arrangement. For Cu spacing between $x = 0$ and 5 Å, this effective field is negative inducing an antiparallel alignment between
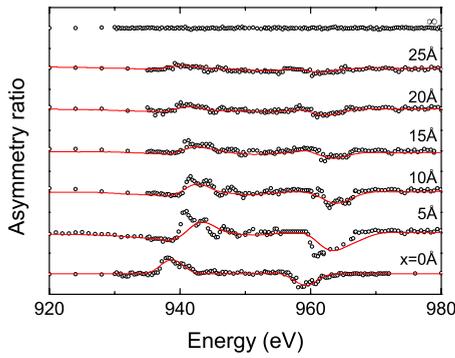
FIG. 6. (Color online) Comparison of the experimental asymmetry ratios (R) measured at the Cu $L_{2,3}$ edges for the multilayers (open circles) and simulation (solid lines).

FIG. 8. (Color online) Hysteresis loops at the Co and Mn L_3 edges (778 eV and 639 eV, respectively) as a function of Cu spacer thickness. Solid lines and symbols are the loops of Co and Mn, respectively.

the Mn and Co atoms. For $x \geq 10$ Å, the effective field is positive inducing a parallel alignment between the Mn and Co atoms. As the XRMS technique is sensitive to both the structural and magnetic contributions the observed asymmetry ratios can be different even though the magnetic structure is similar (see, for example, Fig. 7).

Direct evidence of the change in coupling with Cu spacer thickness is confirmed by the measurements of the XRMS hysteresis loops at the Co and Mn L_2 edges shown in Fig. 8. The Mn loops fit remarkably well to the Co loops clearly indicating that the Co magnetization is responsible for the spin polarization of the Mn. The Co moment is always aligned parallel to the applied field indicating that the magnetization of the Co layers is greater than that induced in the Mn. The hysteresis loops also show the reversal of the sign of the coupling between the Co and Mn. The Mn atoms are coupled antiferromagnetically with the Co layer below $x = 10$ Å and ferromagnetically coupled above. In particular, we note the small size of the measured Cu dichroic effect, indicating the extreme sensitivity of the XRMS technique to small magnetic moments although it was not possible to observe a hysteresis loop for Cu. In order to provide a quantitative explanation and extract the magnetic moment from the reflectivity, the asymmetry data have been analyzed using the model explained in Sec. III. The spectra were calculated using a magnetic multiplying factor for each slice of the interfacial structures containing Mn and Cu given that the XMCD

signal is directly proportional to the magnetic moment. This magnetic factor is used to reduce or increase the magnetic contribution to the reflectivity in order to fit our data. Figures 6 and 7 show the simulations of the asymmetry ratio as a function of the energy at the Cu and Mn $L_{2,3}$ edges for all multilayers. The model reproduces the main features of the experimental data (solid lines in Figs. 6 and 7). The resultant profile of the induced magnetization within the Mn and Cu component of all the multilayers are shown in panels (b), (d), (f), (h), (j), and (l) of Fig. 5 and are scaled to the relative densities in each slice. The profiles have then been normalized to the total magnetic moment to give the induced Mn and Cu magnetization in units of μ_B/atom. We observe that the polarization occurs mainly when the Mn and Cu atoms are close to the cobalt layer and the induced magnetization of the Mn and Cu falls off rapidly away from the Co layer. At the interface, the magnetic moment of the Cu is found to be ≈ 0.05 μ_B, this value is equivalent to the value found in the literature in Co/Cu multilayers.[34] The enhanced Cu d moment near the interface is the result of a considerable hybridization of the Cu and Co 3d orbitals near the interface.[34] For the Mn, the value of the magnetic moment is ≈ 0.3 μ_B and decreases with increasing copper thickness indicating the dominant interfacial nature of the Mn spin polarization (Fig. 5). Furthermore, the Mn polarization switches from an antiparallel alignment with the Co to parallel as the copper layer thickness exceeds $x \geq 10$ Å. This value is consistent with the RKKY coupling period in Co/Cu multilayers.[7]

To better understand our observations we performed a theoretical study of the polarization of cobalt, copper, and manganese in idealized Co/Cu/CuMn multilayers which consisted of a sharp interface region and a lattice-matched superstructure. To calculate the relevant quantities, we have used the density-functional theory (DFT) (Refs. 41 and 42) in the framework of the projector augmented wave (PAW) method,[43] as implemented in the Vienna *ab initio* simulation package (VASP).[44] The PAW method is a very powerful tool for performing electronic-structure calculations within the framework of the DFT. It takes advantage of the simplicity

FIG. 7. (Color online) Comparison of the experimental asymmetry ratios (R) measured at the Mn $L_{2,3}$ edges for the multilayers (open circles) and simulation (solid lines).

of pseudopotential methods but describes correctly the wave function in the augmentation regions. Since this computational method has been described at length before,[43] it is not presented here, but it is worth mentioning that it is a full potential and all-electron method, used widely to investigate the magnetic properties of materials. The Perdew-Burke-Ernzerhof[45] variant of the generalized gradient approximation (GGA) was used for the exchange-correlation potential. Strong correlation effects were taken into account by adding a Hubbard term to the GGA potential, known as the DFT+U method.[46] Values of $U = 4$ eV and $J = 0.9$ eV were used, which are standard values in the framework of this method.[47] Convergence of the total energy was ensured by using a cutoff of 500 eV for the plane-wave expansion of the wave function. To simulate the experimental system as closely as possible within our computational resources, we have built a supercell containing four hexagonal layers of cobalt, stacked in an *AB-AB* fashion, and 11 hexagonal layers of copper, stacked in an *ABC-ABC* fashion (like fcc copper). Then, copper atoms were substituted by manganese at various positions (see below). For each system studied, the geometry of the cell was completely relaxed (volume, cell shape, and positions of the atoms within the cell) so that interface reconstruction, lattice mismatch, and substitutional effects on the electronic structure are fully taken into account. The Brillouin zone was meshed by an $8 \times 8 \times 1$ mesh during the relaxation procedure, then a final run using the relaxed geometry and a $16 \times 16 \times 1$ mesh was performed in order to obtain precise total energies and density of states.

Before studying the Co-CuMn system, we made preliminary calculations on the CuMn system. We setup a supercell with four atoms of Cu and four atoms of Mn in a fcc geometry, and relaxed completely the system. All the parameters used are the same as described above. We found that the ground-state magnetic configuration is antiferromagnetic. The Mn d orbitals are populated with slightly more than five electrons so that each atom has a spin moment of ≈ 3.8 μ_B. As a result of the polarization of the Mn atoms, a magnetic moment is induced on the Cu atoms, of ≈ 0.05 μ_B on the d orbitals. Then, we studied the Co/Cu system without any Mn. We found that the ferromagnetically ordered cobalt layers induce a polarization of the copper atoms near the interface. The magnetic moment on the cobalt atoms have an averaged value of 2.0 μ_B and the induced magnetic moment on the first layer of copper (next to the cobalt) is ≈ 0.02 μ_B on the d orbitals and is parallel with the cobalt moment (ferromagnetic ordering). The magnetic moment of the second layer is decreased and reaches almost zero for the third layer. The extracted moment and spatial decay are consistent with our experimental observations. Note that the absolute values of the induced magnetic moments on the copper atoms are quite difficult to state since they depend on the fine details of the calculations, in particular, the radius of the sphere around each atom used to integrate the density is arbitrary (in our case we have used the default values provided by the code).

Finally, we have introduced two Mn atoms in our system, by replacing two Cu atoms, and we have varied the distance between them by intercalating from zero to four layers of copper. For each configuration, three possible magnetic or-
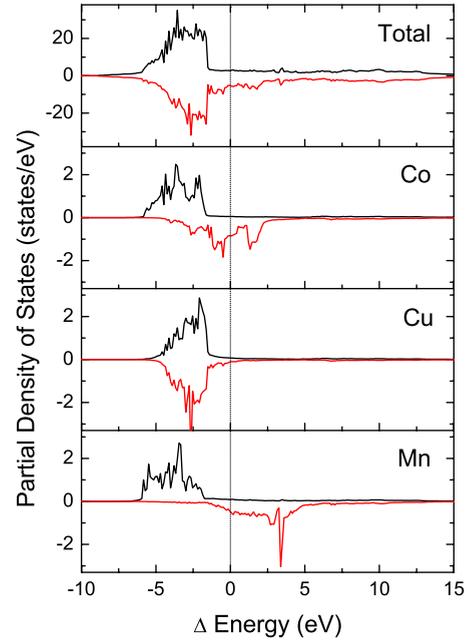
FIG. 9. (Color online) Computed total density of states of the Co-CuMn system (top plot) for an antiferromagnetic alignment between the Mn atoms. The remaining panels display the PDOS for the cobalt atom at the interface (second top plot), the copper atom at the interface (second picture from bottom), and a manganese atom (bottom picture).

ders were checked: either the two manganese atoms are coupled to each other antiferromagnetically or they are coupled ferromagnetically, with the magnetic moments in the same direction as those the Co atoms, or in the opposite direction. Over these three possibilities, we found that the magnetic moments carried by the Mn atoms are ordered preferably in an antiferromagnetic way. In Fig. 9, we show our computed total density of states of the system (top plot), as well as the partial density of states (PDOS) for the cobalt atom at the interface (second top plot), the copper atom at the interface (second picture from bottom), and a manganese atom (bottom picture). The data presented in Fig. 9 are for an antiferromagnetic coupling of the two Mn atoms and represent the lowest total energy for the system. We show the Mn PDOS for the atom aligned parallel to the Co atom. The PDOS for the Mn aligned antiparallel to the Co is very similar, i.e., the spin-up PDOS of one of the Mn atoms being the spin-down PDOS of the second Mn. The Fermi level is set at 0 eV. In this case, the two Mn atoms are in neighboring positions. As expected, the total density of states shows a large magnetic moment for the cell because of the ferromagnetically ordered cobalt layers. More interesting is the magnetic moment carried by the d orbitals of copper atom near the interface, which is ≈ 0.02 μ_B, and parallel to the Co magnetic moment. Therefore, the presence of Mn atoms does not modify significantly the interaction between the cobalt atoms and the layer of copper at the interface. As for Mn in the CuMn system (see above) the majority spin direction of Mn is completely filled by electrons while the minority spin direction is partially filled (see Fig. 9). From these calculations, the Mn atoms are predicted to be antiferromagnetic

with a magnetic moment of ≈ 3.9 μ_B, a value close for a single atom (5 μ_B), but were found to be considerably larger than those determined experimentally using superconducting quantum interference device (SQUID) magnetometry (0.8 μ_B) with a maximum magnetic field of 5 T and T =10 K.

This zero-temperature calculation is consistent with both the absence of the magnetization along the external applied field direction during the XRMS measurements for a pure CuMn sample and the induced magnetization by the cobalt layer. The latter seems to be antiferromagnetically coupled from the interface to within four atomic planes and ferromagnetically in the central CuMn layer. The antiferromagnetic coupling between Co and Mn is experimentally supported by ^{55}Mn NMR from Co/Mn-sputtered multilayers.[48] The spatial dependence of the Cu-induced magnetic moment is predicted to fall away very quickly from the maximum value so that within two atomic planes (≈ 5 Å), it is almost zero. In this respect, the calculations and experimental data are in good agreement for the copper and manganese.

V. DISCUSSION

First, the structural profiles shown in Fig. 5 using soft x rays are consistent with the fits using the hard x-ray technique indicating the robustness of the analysis procedure in extracting the interfacial profiles of the Co/CuMn and Co/Cu interfaces. The Gaussian distribution of the roughness used in the model from the hard x rays show that the resultant profile is found to be identical to that from the fitting strategy of the soft x rays. Significantly, the introduction of the CuMn layers does not alter the physical interfacial structure.

It is informative to look more closely at the spatial and spectroscopic structure which is evident in Figs. 5–7. The Cu polarization is seen to decay rapidly away from the interface (in agreement with our DFT calculations) and to change sign. While the magnitude of the Cu polarization is small away from the interface the change in sign is consistent with the short-period oscillation expected from the Cu Fermi-surface neck spanning vector.[49] Unfortunately, the present experimental resolution prevents us from observing further oscillations in the extracted Cu profile. Closer inspection of the Cu XMCD (Fig. 6) reveals structure in the experimental data not replicated by the simulation. Given the quality of Cu optical constants used in the simulation this is not surprising. In principle, there is also the possibility of separating out the Cu XMCD contribution from pure Cu and CuMn. Furthermore, a higher quality determination of the Cu optical constants, as obtainable at a third generation x-ray source, would presumably allow a refinement of the simulation to capture any more subtle physical effects.

The Mn moment decays rapidly away from the interface with increasing Cu thickness. Also, the Mn polarization is approximately symmetric about the middle of the spacer layer as would be expected for a ferromagnetic alignment of the Co layers. The value of the magnetic moment of the manganese atoms experimentally extracted from the XRMS measurements is small compared to the maximum moment possible for the pure $3d^5$ high-spin ground state.[50–53] The low

magnetic moment could suggest that the ground state is not a high but low-spin state.[54] This is supported by the shape of Mn XAS spectrum (Fig. 3) which does not show the multiplet structure associated with a pure high-spin d^5 state. The DFT calculations also predict a large Mn moment (antiferromagnetically coupled). This high-spin d^5 state gives a significantly larger moment compared to 0.8 μ_B/Mn that we determined experimentally using SQUID magnetometry with a maximum magnetic field of 5 T and T=10 K. Kouvel's[55] model and Smit *et al.*[56] from an experimental analysis interpreted their results in terms of a compensation of certain Mn moments which are antiferromagnetically coupled with nearest-neighbor Mn atoms. Smit *et al.* have shown clear evidence for magnetic clusters and short-range antiferromagnetic interactions where the fraction of the Mn atoms participating in the strongest antiferromagnetic interaction acting from 25 T is estimated to be $\approx 60\%$. According to this study less than 20% of the Mn atoms would be saturated when the sample was subject to a maximum external magnetic field of 5 T. This would correspond to a magnetic value ≈ 3.9 $\mu_B/5 \approx 0.8$ μ_B, a value very close to our value found using bulk magnetometry. Also, Cable[57] found that for 10–20 % Mn in Co alloys, a Mn moment of ≈ 0.3 μ_B aligned antiparallel to the Co. This is consistent with our results for both the magnitude and orientation of the Mn in proximity to the Co.

The weak observed value of the Mn magnetic moment is not surprising since it is averaging over still largely disordered moments that are only slightly preferentially aligned by the exchange field of the cobalt. We can estimate simply the magnitude of this effective indirect exchange field from the bulk room-temperature susceptibility of CuMn.[19] The calculated field is then a factor of ≈ 5 lower than that observed in Co/Cu multilayers[7] with a 9.3 Å Cu spacer. Given the idealized simplicity of the calculation and that our spacer thickness was ≈ 11–12 Å (see Table I), this is a reasonable agreement and would be consistent with the half-filled d states and high-spin configuration.

The DFT calculations reproduce many of the features observed in our experiments: namely, the rapid decay in Cu and Mn polarization with distance from the Co layer, the sign and magnitude of the Cu polarization and the large high-spin moment is consistent with SQUID magnetometry. The DFT calculations predict antiferromagnetic coupling between the Mn atoms which is consistent with our SQUID observations at low temperature. The XRMS measurements were performed at room temperature where bulk CuMn is known to be paramagnetic.[19] This is also confirmed by SQUID measurements. In both cases, the effective field from the Co induces a small Mn ferromagnetic signal through a partial alignment of the Mn paramagnetic arrangement. It is worth noting that in this experiment the Mn is intended simply as a sensing layer but it is clear that there exists substantial scope for further experimental and theoretical study of the interfacial ordering of such alloys.

VI. CONCLUSIONS

Magnetic-charge interference scattering has been used to determine the spatial profile of the magnetic polarization of

the Mn and Cu atoms induced by proximity to a Co layer. Agreement between the calculation and experiment could be achieved through the introduction of extended rough regions at the interfacial boundaries. The Mn and Cu polarizations are predominantly at the low Cu and Mn concentrations end of the interface, in close proximity to the Co and decays rapidly as a function of depth toward the center of the CuMn layer. The Mn polarization is much higher than that of Cu. The Mn atoms are coupled antiferromagnetically with the Co layer below $x = 10$ Å and ferromagnetically coupled above. In contrast, the interfacial Cu atoms remain ferromagnetically coupled to the Co layer for all thicknesses studied as supported by DFT calculations but change sign for larger distances from the polarizing Co layer. Evidently the Mn sensing scheme is a very useful probe for spatially observing small induced moments in layered systems. Having estab-lished the element-specific polarization profile in the proximity case (and the experimental sensitivity) it is now possible to consider extending these measurements to the spin accu-mulation state for which the polarization and lengthscale may be comparable.

*Present address: Physics Department, University of Kiel, Ger-many; abes@physik.uni-kiel.de

†http://www.isis.rl.ac.uk/

‡Present address: FZD Dresden-Rossendorf, Institute of Ion Beam Physics and Materials Research, Dresden, Germany.

[1] I. Žutić, J. Fabian, and S. Das Sarma, Rev. Mod. Phys. **76**, 323 (2004).

[2] D. D. Awschalom and M. E. Flatte, Nat. Phys. **3**, 153 (2007).

[3] A. Brataas, Y. Tserkovnyak, G. E. W. Bauer, and B. I. Halperin, Phys. Rev. B **66**, 060404 (2002).

[4] C. E. Moreau, I. C. Moraru, N. O. Birge, and W. P. Pratt, Jr., Appl. Phys. Lett. **90**, 012101 (2007).

[5] T. Kimura, J. Hamrle, and Y. Otani, Phys. Rev. B **72**, 014461 (2005).

[6] S. S. P. Parkin, N. More, and K. P. Roche, Phys. Rev. Lett. **64**, 2304 (1990).

[7] S. S. P. Parkin, R. Bhadra, and K. P. Roche, Phys. Rev. Lett. **66**, 2152 (1991).

[8] T. G. Walker, A. W. Pang, H. Hopster, and S. F. Alvarado, Phys. Rev. Lett. **69**, 1121 (1992).

[9] R. Springell, F. Wilhelm, A. Rogalev, W. G. Stirling, R. C. C. Ward, M. R. Wells, S. Langridge, S. W. Zochowski, and G. H. Lander, Phys. Rev. B **77**, 064423 (2008).

[10] M. Johnson and R. H. Silsbee, Phys. Rev. Lett. **55**, 1790 (1985).

[11] P. C. van Son, H. van Kempen, and P. Wyder, Phys. Rev. Lett. **58**, 2271 (1987).

[12] M. Ali, C. H. Marrows, and B. J. Hickey, Phys. Rev. B **77**, 134401 (2008).

[13] V. Chakarian, Y. U. Idzerda, C. C. Kao, and C. T. Chen, J. Magn. Magn. Mater. **165**, 52 (1997).

[14] C. Kao, J. B. Hastings, E. D. Johnson, D. P. Siddons, G. C. Smith, and G. A. Prinz, Phys. Rev. Lett. **65**, 373 (1990).

[15] M. Sacchi and A. Mirone, Phys. Rev. B **57**, 8408 (1998).

[16] M. Sacchi, A. Mirone, C. F. Hague, P. Castrucci, R. Gunnella, and M. De Crescenzi, Phys. Rev. B **64**, 012403 (2001).

[17] L. Giovanelli, G. Panaccione, G. Rossi, M. Fabrizioli, C. S. Tian, P. L. Gastelois, J. Fujii, and C. H. Back, Appl. Phys. Lett. **87**, 042506 (2005).

[18] O. Rader, W. Gudat, C. Carbone, E. Vescovo, S. Blügel, R. Kläs-ges, W. Eberhardt, M. Wuttig, J. Redinger, and F. J. Himpsel, Phys. Rev. B **55**, 5404 (1997).

[19] P. Gibbs, T. Harders, and J. Smith, J. Phys. F: Met. Phys. **15**, 213 (1985).

[20] J. Zak, E. R. Moog, C. Liu, and S. D. Bader, J. Magn. Magn. Mater. **89**, 107 (1990).

[21] C.-C. Kao *et al.*, Phys. Rev. B **50**, 9599 (1994).

[22] L. Sève *et al.*, J. Magn. Magn. Mater. **148**, 68 (1995).

[23] N. Jaouen, G. van der Laan, T. K. Johal, F. Wilhelm, A. Rogalev, S. Mylonas, and L. Ortega, Phys. Rev. B **70**, 094417 (2004).

[24] N. Jaouen *et al.*, Phys. Rev. B **66**, 134420 (2002).

[25] J. P. Hannon, G. T. Trammell, M. Blume, and D. Gibbs, Phys. Rev. Lett. **61**, 1245 (1988).

[26] B. Henke, E. Gullikson, and J. Davis, At. Data Nucl. Data Tables **54**, 181 (1993).

[27] L. G. Parratt, Phys. Rev. **95**, 359 (1954).

[28] A. Mirone, ftp://www.esrf-fr/pub/scisoft/ESRF_sw/linux_i386_00

[29] M. Wormington, T. P. A. Hase, B. K. Tanner, and D. K. Bowen, Philos. Mag. Lett. **74**, 211 (1996).

[30] M. Wormington, K. M. Matney, and D. K. Bowen, Philos. Trans. R. Soc. London, Ser. A **357**, 2827 (1999).

[31] C. H. Marrows, N. Wiser, B. J. Hickey, T. P. A. Hase, and B. K. Tanner, J. Phys.: Condens. Matter **11**, 81 (1999).

[32] A. Paul, T. Damm, D. E. Bürgler, S. Stein, H. Kohlstedt, and P. Grünberg, J. Phys.: Condens. Matter **15**, 2471 (2003).

[33] C. T. Chen, Y. U. Idzerda, H.-J. Lin, N. V. Smith, G. Meigs, E. Chaban, G. H. Ho, E. Pellegrin, and F. Sette, Phys. Rev. Lett. **75**, 152 (1995).

[34] M. G. Samant *et al.*, Phys. Rev. Lett. **72**, 1112 (1994).

[35] H. A. Dürr, G. van der Laan, D. Spanke, F. U. Hillebrecht, and N. B. Brookes, Phys. Rev. B **56**, 8156 (1997).

[36] Y. Teramura, A. Tanaka, and J. Takeo, J. Phys. Soc. Jpn. **65**, 1053 (1996).

[37] W. L. O'Brien and B. P. Tonner, Phys. Rev. B **50**, 2963 (1994).

[38] S. Andrieu, M. Finazzi, P. Bauer, H. Fischer, P. Lefevre, A. Traverse, K. Hricovini, G. Krill, and M. Piecuch, Phys. Rev. B **57**, 1985 (1998).

[39] S. Andrieu, E. Foy, H. Fischer, M. Alnot, F. Chevrier, G. Krill,

and M. Piecuch, Phys. Rev. B **58**, 8210 (1998).

[40] J. Dresselhaus, D. Spanke, F. U. Hillebrecht, E. Kisker, G. van der Laan, J. B. Goedkoop, and N. B. Brookes, Phys. Rev. B **56**, 5461 (1997).

[41] P. Hohenberg and W. Kohn, Phys. Rev. **136**, B864 (1964).

[42] W. Kohn and L. J. Sham, Phys. Rev. **140**, A1133 (1965).

[43] P. E. Blöchl, Phys. Rev. B **50**, 17953 (1994).

[44] G. Kresse and D. Joubert, Phys. Rev. B **59**, 1758 (1999).

[45] J. P. Perdew, K. Burke, and M. Ernzerhof, Phys. Rev. Lett. **77**, 3865 (1996).

[46] O. Bengone, M. Alouani, P. Blöchl, and J. Hugel, Phys. Rev. B **62**, 16392 (2000).

[47] K. Sato, P. H. Dederichs, H. Katayama-Yoshida, and J. Kudrnovsky, J. Phys.: Condens. Matter **16**, S5491 (2004).

[48] T. Thomson, P. C. Reidi, Q. Wang, and H. Zabel, J. Appl. Phys. **79**, 6300 (1996).

[49] J. Mathon, A. Umerski, M. Villeret, and R. B. Muniz, Phys. Rev. B **59**, 6344 (1999).

[50] A. Kimura, T. Kanbe, T. Xie, S. Qiao, M. Taniguchi, T. Muro, S. Imada, and S. Suga, Jpn. J. Appl. Phys., Part 1 **42**, 4692 (2003).

[51] W. L. O'Brien and B. P. Tonner, Phys. Rev. B **51**, 617 (1995).

[52] S. Asanao, A. Kimura, T. Kambe, T. Xie, S. Qiao, T. Muro, S. Imada, S. Suga, and M. Taniguchi, Physica B **351**, 355 (2004).

[53] B. T. Thole, R. D. Cowan, G. A. Sawatzky, J. Fink, and J. C. Fuggle, Phys. Rev. B **31**, 6856 (1985).

[54] Y. Yonamoto, T. Yokoyama, K. Amemiya, D. Matsumura, and T. Ohta, Phys. Rev. B **63**, 214406 (2001).

[55] J. S. Kouvel, J. Phys. Chem. Solids **24**, 795 (1963).

[56] J. J. Smit, G. J. Nieuwenhuys, and L. J. de Jongh, Solid State Commun. **31**, 265 (1979).

[57] J. W. Cable, Phys. Rev. B **25**, 4670 (1982).